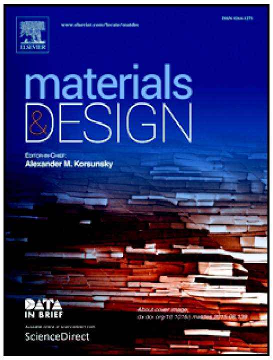

Challenging thermal management by incorporation of graphite into aluminium foams

L.P. Maiorano, J.M. Molina

PII: S0264-1275(18)30641-5
DOI: doi:10.1016/j.matdes.2018.08.026
Reference: JMADE 7324

To appear in: *Materials & Design*

Received date: 24 May 2018
Revised date: 31 July 2018
Accepted date: 12 August 2018

Please cite this article as: L.P. Maiorano, J.M. Molina , Challenging thermal management by incorporation of graphite into aluminium foams. Jmade (2018), doi:10.1016/j.matdes.2018.08.026

Challenging thermal management by incorporation of graphite into aluminium foams

L.P. Maiorano[a], J.M. Molina[a,b *]

[a] Instituto Universitario de Materiales de Alicante, University of Alicante, Ap. 99, E-03080 Alicante, Spain

[b] Departamento de Química Inorgánica de la Universidad de Alicante, University of Alicante, Ap 99, E-03080 Alicante, Spain

ABSTRACT

The recent progress made in active thermal management for electronics demands the development of new open-pore foam materials with excellent thermal performance that result from the combination of high thermal conductivity (≥70 W/mK) and the lowest possible fluid pressure drop. The foams considered to date in the literature do not meet these conditions. In this work, a new class of two-phase composite foam materials, which contain graphite flakes and aluminium, were fabricated by the gas pressure liquid metal infiltration method. These materials were fabricated in two main microstructures: i) aluminium foam with oriented graphite flakes in struts; ii) alternating layers of oriented graphite flakes and aluminium foam. The resulting materials exhibited thermal conductivities within the 60-290 W/mK range, and power dissipation capacities up to 325% higher than those for conventional aluminium foams, with pressure drops kept at convenient values for the most demanding active thermal management applications.

Keywords: metal foam, graphite flakes, infiltration, thermal conductivity, thermal management.

*corresponding author
e-mail: jmmj@ua.es; Tel: +34 965903400 (2055)

1. Introduction

The development of new electronic devices and circuitry of the most innovative technological equipment in electronics, aeronautics and aerospace is concomitant with research into new ways to remove excess heat generated by these devices running normally **[1,2]**. Thermal management allows increasing the reliability of electronic devices while avoiding premature failures. For efficient heat removal from electronic systems, two main strategies have been developed. One, the so-called passive thermal management, comprises driving heat from hot spots to other parts where convective transport processes can easily remove it. A second successful strategy, namely active thermal management, consists in forcing heat to be directly transferred from hot spots to some carrier fluids by a conduction-convection mechanism. A significant number of research groups are developing materials for thermal management based on these two discussed strategies.

Research into new materials for active thermal management has focused mainly on metal and carbon/graphite foams as they show interesting physical properties, such as low density and high specific area per unit volume, plus decent thermal conductivity **[3-8]**. Several foam manufacturing techniques have been developed in the last years **[9,10]**. However, one of the most interesting is the replication method, used traditionally to produce metal foams **[11,12],** which has been recently adapted to fabricate carbon/graphite foams **[13]**. This technique is based on using a template preform, infiltrated by molten metal or a liquid graphite precursor which is then eliminated by either dissolution or a controlled reaction to leave a foam material with a porous structure that replicates the original template preform. The replication method allows the perfect control of size, shape and size distribution of pores. Depending on the matrix material and the desired final pore architecture, different raw materials have been used as templates. However, the most widespread template material has been sodium chloride particles, which can be conveniently packed and infiltrated with liquid metals at temperatures below its melting point (801ºC) to then be removed by dissolution in aqueous solutions. The thermal properties and heat dissipation capacity of the aforementioned conventional foams have been widely studied in recent decades. Many authors have focused on researching forced convection parameters, such as heat transfer coefficient and pressure drop for different metal foams **[4,5,7].** Although their findings are interesting, they do not make up a whole body of references by which new designs of open-cell foam materials can be derived. Nevertheless, one of the main relevant ideas that stems from the still narrow range of foams tested to date is that the best performance is obtained with low-porosity volume fractions (high-volume fraction solid) **[4]**. In this scenario, recent developments have indicated the excellent heat dissipation capacity of magnesium foams with a 0.56 pore volume fraction containing highly thermal conductive diamond particles in struts **[14]**. The few articles published in the literature on the heat dissipation capacity of graphite foams do not offer a better scenario, since their performance is close to that of metal foams when equivalent foams are compared (this is, similar open porosity and solid structure) **[8,15]**. Graphite foams have, moreover, additional drawbacks: their thermal conductivity decreases abruptly with temperature **[16]**, their mechanical properties are poor (tensile strengths are 4-40% of those of metal foams with comparable porosities **[17]**) and their production costs are still excessive, being only suited for high-end niche markets **[18]**.

At the forefront of research into materials for passive thermal management is the development of interfacial-engineered most innovative aluminium/diamond composites, with thermal conductivity around 500 W/mK, which can further increase under precise processing control **[19-20]**. Another group of promising materials are metal matrix composites based on graphite flakes (Gf) given their low density, easy machinability, low price and high thermal conductivity. The control of orientating and distributing Gf in the metal matrix is crucial as they present high anisotropy in thermal conductivity. In this class of materials, Prieto et al. **[21,22]** developed new ternary composites by combining a metal matrix with ceramic particles and graphite flakes, in order to achieve thermal performance (thermal conductivity and coefficient of thermal expansion) that come close to that of metal-diamond composites. These authors reported thermal conductivities above 360 W/mK for Al-12%wt.Si matrix ternary composites by mixing Gf and SiC, where ceramic particles acted mainly as spacers of Gf by allowing metal infiltration.

In the present work a new family of two-phase aluminium matrix composite foam materials were designed, fabricated and characterized. These materials were inspired in the recently developed family of highly anisotropic thermally conductive composites formed by the combination of Gf, ceramic particles and a metal matrix **[21,22]**. The present work combines the appeal of using Gf to enhance thermal conductivity with the advantages that metal foams offer for manufacturing a new family of foam materials for active thermal management applications. The new foam materials are fabricated by replacing the ceramic particles from ternary composites with sodium chloride particles, which act as templates and can then be removed by dissolution to obtain an interconnected pore structure material. The resulting foams present two different limiting microstructures depending on their phases distribution: i) microstructures consisting of a homogeneous distribution of oriented graphite flakes along the porous material; ii) microstructures with alternating layers of oriented graphite flakes and metal foam. Materials were characterized by thermal conductivity, permeability, pressure drop and power dissipation under conditions that emulate real applications. The experimental thermal conductivity results were predicted by developing two analytical models in accordance with both limiting ideal microstructures. The best thermal performance was obtained for the materials with a microstructure of alternating layers of Gf and Al foam. Their thermal conductivity was measured as being up to 290 W/mK and their power dissipation went above 50 kW/m^2 for forced air fluxes of 7.5 l/min, which makes this material and others that perform similarly serious candidates for active thermal management in electronic applications.

2. Experimental procedures

2.1. Fabrication of foams

High purity aluminium (99.999 wt.%) and natural graphite flakes (10 mesh in size) with a purity higher than 99.9 wt.% were supplied by Alfa Aesar (GmbH & Co KG - Karlsruhe, Germany). As shown in Figure 1a, graphite flakes were platelets with an average diameter of roughly 1000 µm and 20-45 µm thickness. Sodium chloride particles of analytical grade (99 wt.%) were purchased from Panreac Química S.L.U. (Barcelona, Spain). The raw NaCl powder was sieved and two fractions were kept to prepare preforms with sizes ranges 80-100 µm and 355-500 µm. Their morphologies are illustrated in Figures 1b and c, respectively.

Al/Gf foams were fabricated by the replication technique. Two kinds of preforms were prepared by different methods depending on the required microstructure: i) Preforms A, with a homogeneous distribution of the oriented Gf and NaCl particles; ii) Preforms B, with alternating layers of oriented Gf and NaCl particles.

Preforms A were prepared as follows. The appropriate amounts of NaCl particles and Gf were mixed by physical agitation. Mixtures were placed inside a mould (10 x 10 x 50 mm) and were delicately subjected to vibrations for 10 seconds to obtain an optimal orientation of Gf. Longer times were checked to produce particle segregation **[22-24]**. Different pressures (depending on the sample) were applied in a perpendicular direction to the oriented Gf for 30 seconds using a manual hydraulic workshop press. In this way, NaCl particles accomplished two main functions: they acted as not only spacers between Gf by allowing liquid metal infiltration, but also as a template to generate a porous structure in the foam material.

Preforms B were prepared by the following procedure. NaCl particles were packed in a mould (10 x 10 x 50 mm) by applying 2.5 MPa with the help of a hand-pressing machine, which resulted in monoliths of packed NaCl particles. Monoliths of highly packed Gf were obtained by the same procedure. Afterwards, monoliths of NaCl and Gf were placed in alternating layers and packed by pressing them (up to 2.5 MPa) with a manual hydraulic workshop press.

The next fabrication step consisted in liquid aluminium infiltration, performed by the gas pressure infiltration technique **[25,26]**. Preforms were placed inside quartz tubes (110 mm high and 16.5 mm inner diameter) previously coated with graphite paint (Condat Lubrifiants, Chasse sur Rhône, France). The empty space between the preform and the tube was filled with packed activated carbon, which kept the sample in place during infiltration. Solid aluminium pieces were placed inside tubes at the top of the compacted samples. Tubes were then introduced inside a pressure chamber and vacuum was dropped to 2 mbar to reduce extraporosity in samples and to prevent metal oxidation. Subsequently, the chamber was heated up to 760^{o}C at a heating rate of 4.5^{o}C/min. After 10 minutes at constant temperature, the vacuum was closed and argon was applied until a 10 bar pressure was reached. After infiltration, the whole chamber was cooled down under rapid solidification conditions (50ºC/min).

Samples were then extracted by machining away the surrounding infiltrated activated carbon. Finally, the NaCl interconnected particles were removed by dissolution. Dissolving the template was carried out in a two-step process: firstly, samples were immersed in distilled water, which was magnetically stirred for 30 minutes at room temperature to facilitate the dissolution of the outermost NaCl particles; secondly, samples were subjected to continuous infiltration with a water flow at 8 bar, which allowed to dissolve the entire template body 10 times faster than under normal dipping conditions. The average NaCl particle diameter and the volume fractions of pore, metal and Gf attained in each sample are available in Table 1.

2.2. Characterization of Al/Gf foams

2.2.1. Microstructural observation and image microstructural analysis

Foam materials were prepared for the microstructural analysis under optical and electronic microscopy by standard metallographic procedures. To prevent plastic deformation during polishing for optical microscopy preparation, they were infiltrated with colourless epoxy resin Resoltech WWA/WWB4 (Rousset, France) at room temperature. After solidification, an epoxy matrix composite slice was cut for grinding and polishing. Silicon carbide grinding papers (Buehler, Illinois, USA) of granulometry P80, P240, P600, P800, P1200 and P2500 were subsequently used for at least 10 minutes each. Finally, samples were polished with Buehler 6 µm diamond paste (Buehler, Illinois, USA) on a MICROMET cloth (Buehler, Illinois, USA) for approximately 20 minutes. Microstructures were characterized by optical microscopy (Olympus PME-3) and Scanning Electron Microscopy (SEM - Hitachi S3000N) operating at 20.0 kV.

Different features of the pore characteristics in the foam materials were accessed by carefully analysing the microscopy images with the help of the image analysis software (Buehler-Omnimet Enterprise, Illinois, USA).

2.2.2. Permeability measurement

Permeability can be simply estimated with injection experiments using water as a fluid. Effective permeability k (m^2) can be calculated if we assume a steady-state regime and a saturated unidirectional flow of an incompressible fluid, according to Darcy's law with the following equation **[5,25]**:

$$k = \frac{\mu Q L}{\pi \cdot r^2 \, \Delta P} \tag{1}$$

where Q is the water flow rate (m^3/s), L is the length of the sample (m), µ is the dynamic viscosity of water (taken as 1.003 $mN \cdot s/m^2$ for water at 20ºC), r is the radius of the sample (m) and ΔP is the differential pressure across the sample (N/m^2). Water flow rate Q can be obtained as the slope of a linear correlation between the water volume outgoing from the sample monitored over time for a given differential pressure. In our experiments the permeability of the Al and Al/Gf foams was obtained by monitoring the mass of water (g) passing over time (s) on a ±0.1 mg precision balance (Precisa ES320A) in a device whose diagram is shown in Figure 2a. For a precise coupling mass and time, the injection experiments were video-recorded with a digital camera (Xiaomi, 13Mpx, ISO127). The inlet air flow was regulated with a ±0.01 bar precision manometer. Negligible water mass losses from the collecting container due to evaporation were discarded as the total time of each measurement took less than 2 minutes.

2.2.3. Thermal conductivity – measurement and the GDEMS model

The thermal conductivity of metal foams was measured by a relative steady-state (equal-flow) technique in an experimental setup assembled in the University of Alicante laboratories according to international standard ASTM E-1225-04 **[20]**. The parallelepiped foams were placed between two blocks, with Gf oriented in a parallel direction to the heat flux. The bottom of the sample remained in contact with a cylindrical cooled base (achieved by a room temperature water flux), and the top of it in contact with a brass reference block connected to a 70^{o}C water bath. Two sets of three and two thermocouples, connected to a reference material and the sample, respectively, allow measuring the temperature gradients to estimate thermal conductivity. Overall uncertainty was estimated to be less than ±5%.

The estimation of the thermal conductivity in the foam materials must consider the specific microstructure at hand. For the microstructures of the materials developed herein, proper models were developed (see the sections below). For the time being we limited our modelling framework to the simple case of foam materials, consisting of randomly distributed monodispersed pores in a metallic matrix, for which the common expression of the GDEMS model can be used **[27]**:

$$K_{mf} = K_m \, . (Vm)^n \tag{2}$$

where K_{mf} and K_m are the thermal conductivities of the metal foam and metal, respectively. Vm is the metal volume fraction, which equals (1-Vp) in a two-phase foam material, with Vp being the pore volume fraction. The n exponent in Equation (2) is a parameter related to the geometry of pores which, for spherical pores, is n=3/2 **[27]**.

2.2.4. Power dissipation density and pressure drop measurement

No standardised methodology exists to test heat sinks in induced-convection active thermal management. The experimental setup used herein (Figure 2b) has already been presented in **[14]** and was inspired in that proposed in **[28]**. In this device, an air flow is forced to pass through a foam sample, which remains in contact with a hot surface so that air can take part of the heat transferred to foam by conduction to remove it by forced convection. The device is equipped with two thermocouples, T_1 and T_2, distanced at 36 mm and located on a brass piece that leads heat from the heating system to the sample. The heating system operates to control the temperature of the T_1 thermocouple at 80ºC. The imposed air flow was regulated by a ±0.1 l/min flow meter at the following values: 2.5, 5, 7.5, 10, 12.5 and 15 (l/min). When a specific air flow was set, the system needed about 15 minutes to reach a steady-state regime, after which temperatures T_1 and T_2 were noted. The thermal gradient in the brass reference piece can be related to the heat dissipation power density P (W/m^2) of the sample by the following equation (equal heat flux through the reference and sample, and negligible heat losses were assumed, provided that the reference was thermally isolated, and both the reference and sample had similar diameters):

$$P = \frac{K_c^b (T_2 - T_1)}{dx} \tag{3}$$

where K_c^b is the thermal conductivity of the reference material (in the present case, K_c^b for 99.99% brass equalled 109 W/mK), T_1 and T_2 are the temperatures measured in the brass block, and dx is the distance between the two thermocouples.

The pressure drop was measured with the same device used for the permeability measurements (Figure 2a) by replacing water with pressurised air along the circuitry. On this occasion, the air flow was followed with an air flowmeter (0-20 l/min), which was placed between the air container and the sample, and pressure was triggered by the manometer.

2.2.5. Flexural modulus

The flexural modulus of the resulting materials was measured using the three-point-bending test with a span of 32 mm and a crosshead speed of 0.1 mm/min. Prior to bending tests, the surface of all samples was polished using SiC paper and diamond paste up to 6 μm grain size. The equipment was calibrated against pure aluminum, for which a flexural modulus of 68.0 GPa, equal to the theoretical value found in the literatura, was obtained.

3. Results and Discussion

3.1. Packing NaCl-Gf preforms – microstructural restrictions for foaming

The packing efficiency of the mixtures of salt particles and Gf is related mainly with the packing pressure used while preparing preforms. Preforms with different contents of NaCl and Gf were processed at a wide variety of controlled packing pressures, which fell within the 0-4.5 MPa range. The calculated volume content of NaCl, Gf and porosity is shown in Figure 3a for Preforms A and in Figure 3b for Preforms B. The plots in Figure 3 are similar but slight differences due to the microstructural feature characteristics of Preforms A and B can be extracted. It is worth mentioning that Preforms B were prepared with a wide variety of thicknesses and proportions of the Gf and NaCl monoliths. However, no signinficant compaction differences were found and the volume fraction curves fulfilled those plotted in Figure 3b.

Preforms A processed at pressures above 3.5 MPa and absence of NaCl particles get fully packed, with no empty space between Gf to allow infiltration. Full packing also occurred for the pressures of 4.5 MPa with contents of NaCl particles reaching up to 60%. Under these conditions, the salt particles that acted as spacers between Gf seemed to be fully covered by Gf, which clearly evidenced Gf deformation, a point that is discussed in-depth later. This effect was not observed in the preforms B, which only became fully dense for high pressures and in the absence of the NaCl particles. This was expected because the Gf and NaCl particles in the Performs B only came in contact with the interlayers of the different monoliths. Hence while Gf could be fully packed in the monoliths, the layers of NaCl particles would transfer their intrinsic porosity to the overall material.

The ulterior step of NaCl dissolution in foam processing led to some restrictions in the phase content of the preforms. To insure that the dissolution process was effective and complete, the NaCl particles needed to form an interconnected network with a coordination number for each particle of at least 3 (a coordination number of 2 could also suffice, but the dissolution time would be longer). Accordingly, and by taking into account the work of Iwata et al. **[29**], in which the statistical distribution of coordination number N was related with the porosity values of the spherical particulate packed preforms, samples had to have pore volume fractions above 0.3, which meant that preform porosities were limited to a maximum value of 0.7. This restriction can be understood as a percolation limit that affects only the samples prepared using Preforms A, which is indicated in Figure 3a as a dotted line. Another restriction is that the sole action of gravity allows certain packing efficiency with no external pressure. This is shown in Figure 3a by the line corresponding to a nominal zero pressure. It was not possible to manufacture the preforms that fell in this area, hence this region defined a compaction limit. For Preforms B, no percolation restriction was applicable as the structure could be ideally understood as being composed of alternating NaCl and Gf monoliths. Let’s take an extreme case in which the volume fraction of the NaCl monoliths is insignificant compared with that of the Gf monoliths, V´NaCl can be very small, but the NaCl particles in the monolith still have enough coordination to be effectively removed. Another compaction limit is detected in this system for the preforms prepared with no external pressure as a result of the natural trend of particles and graphite flakes to lie on top of one another.

3.2. Microstructure, permeability and thermal conductivity of the Al/Gf foams

The main features and properties of the different foam materials fabricated in this work are found in Table 1. Thermal conductivity was measured in the direction of graphite flakes orientation (the so-called longitudinal thermal conductivity, or K_c^L). Materials were classified into four main groups depending on different fabrication parameters. For the sake of comparison, three aluminium foams (in the absence of Gf) were also fabricated by the compaction of NaCl particles at 0.0, 0.7 and 2.0 MPa, respectively. The optical micrographs of some representative samples were analysed (Figure 4). The first image (Figure 4a) is a photograph showing the geometry and dimensions of two of the samples fabricated in this work. The micrographs in Figures 4b and 4e pertain to a sample fabricated with a Preform A and a high content of large salt particles (355-500µm). The orientation of Gf was clearly distorted by the presence of large NaCl particles when a packing pressure was applied to fabricate the preform. This phenomenon was less pronounced for the samples that derived from smaller NaCl particles (80-100mm), where the orientation of Gf was clearly seen (Figures 4c and 4f). The foams that derived from Preform B, for which large NaCl particles (355-500µm) were used, did not evidence any Gf deformation, as it must correspond to a microstructure made up of alternating packings of monoliths of both the packed NaCl particles and Gf (Figures 4d and g). As previously explained, since no spacers were used to prepare the Gf monoliths, some Gf-Gf contacts were solely of a physical nature since metal infiltration to the narrow channels in between them was not possible (Figure 4h).

Figure 5a shows the experimental results of the water volume recorded with time for some injection experiments run to measure permeability k. The k values of the different samples are provided in Table 1. As expected, permeability dropped as the porosity of the material reduced. Plenty of research works have shown interpretations of the permeability of metallic foams. To date, it has been demonstrated that the measured values of permeability adimensionalised by dividing the measured k values by average pore diameter d^2 must collapse onto a single curve when plotted as a function of the foam density **[30]**. Figure 5b shows this representation in which the experimental values defined a curve of the type found for conventional metal foams, independently of the specific microstructure of each sample. Only samples C-1 and C-2 clearly went beyond the general tendency, which was most probably caused by the microstructural inhomogeneities that derived from their high Gf content. In view of the curve's shape, we can state that permeability decreased rapidly above (1-V´p)=0.30 in accordance with **[30]**. We see some salient aspects when focusing on the thermal conductivity data in Table 1. The samples that did not contain Gf (A-1, A-2 and A-3) obtained low thermal conductivity values. The log (K_{mf}) plotted as a function of log (Vm) allowed us to obtain parameter n from the slope of the line in accordance with Equation (2). This plot is shown in Figure 5c, from which it is derived that n=1.52. However this value, which agrees with the close-to-spherical shape of the NaCl particles, is shown in Figure 1c. The attained volume fraction of the NaCl particles for the non-applied compaction pressure (A-3 sample) was 0.61, which was lower than the value of 0.64 attained in **[30]** for the random distribution of spherical powders.

When graphite flakes were present, samples showed higher thermal conductivity, which was proportional to Gf content, and was inversely proportional to porosity content, as inferred from the fact that Gf displayed a higher thermal conductivity than aluminium metal and pores, understood as inclusions of zero nominal thermal conductivity. Both effects are clearly illustrated in Figures 5d and 5e, where the thermal conductivity values for all the samples are plotted against porosity and graphite flakes content, respectively. Figure 5d includes a curve calculated by the GDEMS model (Equation 2) for the thermal conductivity of aluminium foams (without Gf), which encompasses the experimental values encountered for the three fabricated Al foams. Interestingly, all the samples that contained graphite flakes obtained thermal conductivity values above those of the curve for a given V´p. The difference between the experimental and calculated values grew increasingly higher when moving towards lower porosity values. This effect is indicative of the beneficial effect caused by the high thermal conductivity of Gf. Figure 5d does also contain a vertical line that corresponds to the percolation limit explained above, which imposes a limit for foaming the materials prepared from Preforms A. This is why the leftmost region below V´p=0.3 shows only one type KK sample (derived from Preforms B).

The reasoning behind understanding Figure 5d is clearly evidenced in Figure 5e, which represents the dependence of thermal conductivity on Gf content. All the group samples show proportionality between both variables. Nevertheless, the temptation of linearising these behaviours must be done cautiously because thermal conductivity is strongly affected by the specific microstructure at hand which, in turn, depends on the different phase contents. It is interesting to note that the materials which derived from Preforms A (with a homogeneous distribution of the oriented Gf - samples B, C and D) offered, compared to a given graphite content, higher thermal conductivities than those that derived from Preforms B (alternating layers of monoliths of Gf and NaCl - samples KK). The reason for this phenomenon relies on the fact that the Gf monoliths in Preforms B did not contain particles which acted as spacers. Hence the liquid aluminium infiltration to the narrow open space in between flakes was rendered difficult, or even impossible. As a result, the flakes in the monoliths physically touched one another with no surrounding matrix, and the thermal conduction mechanism most probably occurred by poor flake-to-flake heat transmission. Another salient feature of this figure is that those samples which contained smaller sized pores (samples B-1, B-2 and B-3) gave higher thermal conductivity values, which could be related to the possibility indicated in the previous section of Gf possibly deforming around the NaCl particles in the packed preform. This deformation, which was more pronounced around large particles, generated loss of graphite orientation along the preferred plane and, hence, less longitudinal thermal conductivity.

3.3. Modelling permeability in Al and Al/Gf foams

The intrinsic permeability of some Al and Al/Gf foams (Table 1) can be interpreted by taking into account the following expression for the permeability of an open-pore foam material **[31]**:

$$k = \frac{Vp \cdot N \cdot {r_n}^3}{6\pi \cdot \left({}^{d}/_{2} \right)} \tag{4}$$

where r_n is the average radius of the necks between two particles, N is the coordination number and d is the average pore diameter (taken as the average pore diameter of NaCl particles). Parameters N and r_n can be accessed by analysing different micrographs with the help of the image analysis software. Table 2 reports the average N value and the maximum and minimum r_n values measured for the considered samples. Figure 6a is a plot of the r_n measurements taken for sample KK-2.

Figure 6b represents the permeability results, both measured and calculated with Equation (4), by accounting for the two extreme r_n values. As the figure depcits, the values calculated with the minimum r_n better agree with the experimental results, which is most probably due to the narrowest windows of pore interconnexions acting as “bottlenecks” that govern the overall water flow rate. A similar approach of considering the narrowest constrictions to be a flow dominant has been considered in the well-known “lubrication theory” to successfully estimate the permeability of fibre bundles in a cross-flow in high solid volume fractions **[32-34]** and in metal foams with high porous volume fractions **[30]**.

3.4. Modelling thermal conductivity in Al/Gf foams

Two theoretical modelling schemes are proposed in this work to predict the experimental thermal conductivity results of the different Al/Gf fabricated foams. The analytical expressions considered two different ideal microstructures: i) composite foams prepared with Preforms A (model 1, or alternatively M1); ii) composite foams prepared with Preforms B (model 2, or alternatively M2). The schematic diagrams of the idealised microstructures are given in Figure 7. The two microstructures can be understood as being formed by an aluminium foam containing graphite flakes, either in an oriented but random distribution (Preforms A) or by forming alternated layers of flakes and foam (Preforms B). In both cases a two-step calculation procedure can be followed. The first calculation step for both microstructures consists in the calculation of the thermal conductivity of the binary metal-pore system (foam structure) by using the general expression of the GDEMS model for foams (Equation (2)), this time expressed as follows:

$$K_{pmf} = K_m . (V\acute{} m)^n \tag{5}$$

where K_m is the thermal conductivity of the metal (in the present case 99.999% Al, taken as 237 W/mK) and V´m is the metal volume fraction in the pseudo-matrix, which can, in turn, be calculated as:

$$V\acute{} m = \frac{Vm}{Vm + Vp} \tag{6}$$

where Vm and Vp refer to the volume fraction of metal and pores, respectively, in the composite material. Exponent n in Equation (5) can be taken as 1.5 for the NaCl particles used in the present work, as deduced from Figure 5c.

The second calculation step considers the inclusion of the graphite flakes into the foam structures. This is different for each microstructure and so we treat the two cases separately.

3.4.1. Modelling scheme for Preforms A (Model M1)

For the microstructures where Gf are oriented and distributed homogeneously in a matrix, we can take the expression derived by Hatta and Taya **[35]** for longitudinal thermal conductivity K_c^L **[22,36]**:

$$K_c^L = K_{pmf} + K_{pmf} \frac{V\acute{}f}{S_L(1 - V\acute{}f) + \frac{K_{pmf}}{K_f^L - K_{pmf}}} \tag{7}$$

where K_f^L refers to the longitudinal thermal conductivity of Gf (taken as 300 W/mK **[22]**), V´f is the volume fraction of Gf in the composite material and S_L is a factor that considers the geometry of Gf that can be calculated as

$$S_L = \frac{\pi t}{4D} \tag{8}$$

where t and D are the thickness and diameter of Gf, respectively.

3.4.2. Modelling scheme for Preforms B (Model M2)

Model 2 considers the ideal microstructures that derived from Preforms B in which layers of aluminium foam monoliths were alternated with layers of Gf monoliths. In this case, the longitudinal thermal conductivity of composite K_c^L can be estimated by the well-known Maxwell approach **[22,36,37]**:

$$K_c^L = V\acute{}f . K_f^L + (1 - V\acute{}f). K_{pmf} \tag{9}$$

3.4.3. Correllation with the experimental results

According to the thermal conductivity models applied herein, analytical values correlated with the experimental results in Figure 8. Figure 8a illustrates a ternary diagram that contains the curves representing longitudinal thermal conductivity K_c^L calculated with the equations that correspond to model 1 (M1). Once again, the restrictions associated with the compaction and percolation limits are considered. We can see that M1 can reasonably predict the longitudinal thermal conductivities for the Al/Gf foams with the homogeneous distribution of the oriented Gf.

Model 2 (M2) requires a simpler ternary diagram. The analytical longitudinal thermal conductivity K_c^L values are represented as curves in Figure 8b, where the prohibited compositions are restricted to the compaction limit (as shown in Figure 3b). The experimental results confirm that the approaches followed for model 2 can be successfully applied to samples with an alternated layered microstructure.

Models M1 and M2 offer calculated values that are very close for the two microstructures considered. This is due to the fact that, for the large geometries of graphite flakes here considered, both microstructures are thermally equivalent since S_L is so small (=0.016) that the term $S_L(1-V'f)$ in the denominator of Equation (7) can be neglected and, after rearraging, Equation (7) becomes Equation (9). When dealing with other geometries of graphite flakes the former approximation is not applicable and models M1 and M2 would then offer different calculated values. We note in passing that the equations for the two models M1 and M2 are independent of any interface thermal conductance, in line with the findings of **[22]** for the longitudinal thermal conductivity of Al/graphite composites. Figure 9a shows the thermal conductivities calculated with both models M1 and M2 according to the experimental data. In general, the experimental results correlated well with the values calculated with M1 and M2. Both models offered calculated values that come closer for the extreme cases of V´f (V´f=0 and V´f=1) and for high K_{pmf} (Figure 9b). The similitude of the results calculated with both models for the K_{pmf} values considered in the present samples, which varied within the 20-58 W/mK range, revealed a difference between M1 and M2 that fell within the 9%-2% range for V´f=0.5. This means that M2 can be considered a simple, but valid, approach for the rough estimation of the foams with a homogeneous Gf distribution fabricated in this work.

3.5 Power dissipation density and pressure drop

The power dissipation density and pressure drop results obtained under working conditions are represented in Figure 10. The experimental results show increments in power dissipation density up to 325% compared with conventional aluminium foams. Once again, Gf can be considered effective thermal inclusions as they confer better power dissipation performances as the volume fraction of Gf increases. The high Gf content in sample C-1 (the sample with the highest power dissipation density for the homogeneous Gf distribution) is concomitant with a small volume fraction of pores and a pressure drop, which is considerably higher than conventional aluminium foams. Sample KK-1, which contains a smaller pore volume fraction than sample C-1, shows a similar power dissipation density (Figure 10a) and pressure drop (Figure 10b). This effect can be related to their close permeability values (Table 1).

4. Design considerations for heat dissipation under air-forced convection

The design of heat sinks from a given material becomes complicated when its intrinsic properties are anisotropic because the final thermal properties can be size-dependent **[38]**. In addition to anisotropy in thermal conductivity, it should be added that the pumped air used to measure its thermal power dissipation density comes out of preforms at different temperatures, and rushes along the length of the material **[3],** which makes this measurement dependent on the length of the considered sample. To study this effect, new power dissipation measurements were taken by the test setup shown in Figure 2b, and by taking into account a longer sample length of 23 mm (standard tests throughout this study were performed on the 10-mm sample lengths). The new data analysis showed that thermal power dissipation increased in all cases (i.e. in all the samples and for all the studied air flows) compared to the measurements taken for the 10-mm sample lengths. This increment (R) can be defined as:

$$R = \frac{P_{23mm}}{P_{10mm}} \cdot 100 \qquad (10)$$

where P_i is power dissipation density at length i.

Figure 11 shows a contour plot of R as a function of the thermal conductivity of the samples and the air flow conditions. R is a design parameter that tends to be small for any low dependence of power dissipation density on sample geometry. The plot reveals a strong dependency of R with the two variables and allows useful information to be extracted for heat sinking designs, which are herein mentioned.

For thermal conductivities roughly below 100 W/mK, contour curves seem to indicate that minimum R values are obtained for air flows at around 3 l/min. Under these air flow conditions, thermal power dissipation is less dependent on geometry than under other conditions. Hence the design of heat sinking devices to operate with this air flow is less restricted to the geometrical considerations imposed by thermal packaging in the final operating system. R is positive for air flows lower or higher than 3 l/min. This indicates that thicker samples are necessary to enlarge the thermal power dissipation of the materials under active thermal management operating conditions. When considering thermal conductivities above 100 W/mK, R lowers with increasing thermal conductivities and air flows. R=0 (or geometry-independency) can be reached for thermal conductivities above 225 W/mK and for air flows within the 7-10 l/min range. The operating air flow conditions for which R=0 expand for higher thermal conductivities. Two main features are worth mentioning. On the one hand, the fact that R equals zero for such high thermal conductivity values leads to the conclusion that conduction and convection are important mechanisms of heat transport that take place during power dissipation. Air is forced to pass through the foam material, which remains in contact with a hot plate and represents hot spot areas in an electronic device. Thus air can form part of the heat transferred to foam by conduction and can remove it by forced convection. The higher the thermal conductivity of materials, the faster heat can be transferred through the material by conduction and, hence, the heat transfer towards air by convection beomes more effective. On the other hand, Figure 11 shows that the higher the thermal conductivity of the material, the higher the air flow imposed to reach R=0 must be. This agrees with the above conclusion, and also with the fact observed in **[3]** that the higher the imposed air flow, the longer the distance that air can travel inside foam before leaving the material through its sides. Under these conditions of high thermal conductivities, the conduction mechanism is effective in transfering heat further away in the preform, and only high air flows can insure that air can travel long enough inside foam to effectively extract heat along the length of the material. Details of the plot in Figure 11 will most probably change when analysing other sample geometries, but the main salient features remain the same. As a conclusive observation, we state that the design of heat sinks for active thermal management is less restrictive to sample geometry for foam materials with high thermal conductivity. Hence they are simpler to adequately fit the space restrictions that some applications may impose.

Another crucial issue of these materials for its use in real applications is their flexural moduli (values for some slected samples are gathered in Table 1). For samples A-i (with no graphite flakes content), the measured flexural moduli is in the trend of the flexion and compression moduli measured for a wide variety of aluminium replicated foams with a porosity content in the 60-90% range **[39]**. When graphite flakes are present, the measured flexural moduli are not far from those derived for samples A-i, albeit samples have a much lower pore volume fraction. A decrease in mechanical properties of aluminium with the graphite flakes content was measured in **[40]** for Al/graphite flakes composites processed via powder metallurgy. When the same selected samples were tested with an aluminium metal coating on top and bottom parts (this metal coating appears naturally with the infiltration processing and is oftern removed away by machining), emulating sandwich structures, the flexural moduli were about 400% higher than the ones gathered in Table 1.

5. Conclusions

A new family of two-phase composite foams, based on the aluminium and graphite flakes combination, was successfully fabricated by the gas pressure infiltration of liquid aluminium into preforms of packed leachable NaCl particles and gfraphite flakes. By different preform preparation methods, materials with two distinct microstructures were developed: i) aluminium foams with oriented graphite flakes in struts; ii) alternating layers of oriented graphite flakes and aluminium foam. The characterization of both types of materials offers outstanding results in thermal dissipation performance terms: the high longitudinal thermal conductivity of materials, which fell within the 60-290 W/mK range, entails an excellent heat conduction mechanism in the foam structure to allow power dissipation densities that are up to 325% higher than those measured for conventional aluminium foams. The pressure drop of these materials decreases with permeability, which shows the direct dependence on the narrowest sizes of the interconnected windows in metal foams, but within the proper values for the most demanding active thermal management applications. Moreover, two modelling approaches to calculate the thermal conductivity in these materials were considered, based on the two developed microstructures. Given the relatively high graphite flakes contents and their great intrinsic thermal conductivity, the model based on the Maxwell approach, and derived for alternating layers of graphite flakes and aluminium foams (M2 in the text) is as an easy predictive tool for all materials. Finally, it is noteworthy that the excellent heat conduction properties of the developed materials mean that their inherent anisotropy is less important for design considerations in heat sinking thermal packaging. The outstanding thermal properties of the presented materials, along with their reasonably good mechanical properties, encounter no competitor among the existing foams published in the literature, either metallic or graphitic, in the field of light-weight materials for thermal management applications

Acknowledgment

The authors acknowledge partial financial support from the “Ministerio de Ciencia e Innovación” (grant MAT2016-77742-C2-2-P).

Data availability

The raw/processed data required to reproduce these findings cannot be shared at this time as the data also forms part of an ongoing study.

References

[1] Schelling PK, Shi L, Goodson KE. Managing heat for electronics. Mater Today 2005(June):30–5.

[2] Zweben BC. Thermal materials solve power electronics challenges. Power Electron Technol 2006(February):40–7.

[3] Shih WH, Chiu WC, Hsieh WH. Height effect on heat-transfer characteristics of aluminum-foam heat sinks. J Heat Transf 2006;128:530–7.

[4] Zaragoza G, Goodall R. Metal Foams with Graded Pore Size for Heat Transfer Applications. Adv Eng Mater 2012;3:123–8.

[5] Zaragoza G, Goodall R. Development of a device for the measurement of thermal and fluid flow properties of heat exchanger materials. Int J Heat Mass Transf 2014;56:37-49.

[6] Abuserwal AF, Luna EME, Goodall R, Woolley R. The effective thermal conductivity of open cell replicated aluminium metal sponges. Int J Heat Mass Transf 2017;108:1439-48.

[7] Mancin S, Zilio C, Diani A, Rossetto L. Air forced convection through metal foams: Experimental results and modelling. Int J Heat Mass Transf 2013;62:112–23.

[8] Straatman AG, Gallego NC, Yu Q, Betchen L, Thompson BE. Forced convection heat transfer and hydraulic losses in graphitic foam. J Heat Transf 2006;129:1237–45.

[9] Bayolo JM. Open-cell porous metals for thermal management applications: fluid flow and heat transfer. Materials Science and Technology 2017; 33: 265-76.

[10] Mahadev, Sreenivsa CG, Shivakumar KM. A Review on Production of Aluminium Metal Foams. IOPO Conference Series: Material Science and Engineering 2018; 376.

[11] Conde Y, Mortensen A. Age-hardening Response of Replicated Microcellular Al-4.5% Cu. Adv Eng Mater 2008; no 200020:849–52.

[12] Conde Y, Despois JF, Goodall R, Marmottant A, Salvo L, San Marchi C, Mortensen A. Replication processing of highly porous materials. Adv Eng Mater 2006;8:795-803.

[13] Prieto R, Louis E, Molina JM. Fabrication of mesophase pitch-derived open-pore carbon foams by the replication processing. Carbon 2012;50:1904-12.

[14] Molina-Jordá JM. Multi-scale design of novel materials for emerging challenges in active thermal managemenet: Open-pore magnesium-diamond composite foams with nano-engineered interfases. Composites Part A 2018;105:265-73.

[15] Haskell MD. Thermal Resistance Comparison Of Graphite Foam, Aluminum, And Cooper Heat Sinks. Electronic Cooling 2006;12.

[16] Gaies D, Faber KT. Thermal properties of pitch-derived graphite foam. Carbon 2002;40:1131-50.

[17] Lin W, Yuan J, Sundén B. A review on graphite foam as thermal material for heat exchangers.Energy End-Use Efficiency Issues (EEE) 2011; 748-55.

[18] Han XH, Wang Q, Park YG, Joen C, Sommers A, Jacobi A. A Review of Metal Foam and Metal Matrix Composites for Heat Exchangers and Heat Sinks. Heat Transf Eng 2012; 33(12):991-1009.

[19] Monje IE, Louis E, Molina JM. Interfacial nano-engineering in Al/diamond composites for termal management by in situ diamond surface gas desorption. Scripta Mater 2016;115:159-63.

[20] Monje IE, Louis E, Molina JM. Optimizing thermal conductivity in gas-pressure infiltrated aluminium/ diamond composites by precise processing control. Composites Part A 2013;48:9-14.

[21] Prieto R, Molina JM, Narciso J, Louis E. Fabrication and properties of graphite flakes/metal composites for thermal management applications. Scripta Mater 2008;59:11-14.

[22] Prieto R, Molina JM, Narciso J, Louis E. Thermal conductivity of graphite flakes – SiC particles / metal composites. Composites Part A 2011;42:1970-77.

[23] Zhou C, Huang W, Chen Z, Ji G, Wang ML, Chen D, Wang HW. In-plane thermal enhancement behaviors of Al matrix composites with oriented graphite flake alignment. Composites Part B 2015;70:256-262.

[24] Li W, Liu Y, Wu G. Preparation of graphite flakes/Al with preferred orientation and high thermal conductivity by squeeze casting. Carbon 2015;95:545-551.

[25] García-Cordovilla C, Louis E, Narciso J. Pressure infiltration of packed ceramic particulates by liquid metals. Acta Mater 1999;47:4461-79.

[26] Molina JM, Piñero E, Narciso J, García-Cordovilla C, Louis E. Liquid metal infiltration into ceramic particle preforms with bimodal size distributions. Curr Opin Solid State Mater Sci 2005;9:202-10.

[27] Weber L, Fischer C, Mortensen A. On the influence of the shape of randomly oriented, non-conducting inclusions in a conducting matrix on the effective electrical conductivity. Acta Mater 2003;51:495-05.

[28] Hsieh WH, Wu JY, Shih WH, Chiu WC. Experimental investigation of heat-transfer characteristics of aluminium-foam heat sinks. Int J Heat Mass Transf 2004;47:5149-57.

[29] Iwata H, Homma T. Distribution of Coordination Numbers in Random Packing of Homogeneous. Powder Tech 1974;10:79–83.

[30] Despois JF, Mortensen A. Permeability of open-pore microcellular materials. Acta Mater 2005;53:1381-88.

[31] Furman EL, Finkelstein AB, Cherny ML. Permeability of aluminium foams produced by replication casting. Metals 2013;3:49-57.

[32] Sangani AS, Acrivos A. Slow flow past periodic arrays of cylinders with application to heat transfer. Int J Multiphase Flow 1982;8:193.

[33] Sangani AS, Yao C. Transport processes in random arrays of cylinders. II. Viscous flow. Phys Fluids 1988;31:2435.

[34] Keller JB. Viscous flow through a grating or lattice of cylinders. J Fluid Mech 1964;18:94.

[35] Hatta H, Taya M. Equivalent inclusion method for steady-state heat-conduction in composites. Int J Eng Sci 1986;24:1157-72.

[36] Molina JM, Louis E. Materials characterization anisotropy in thermal conductivity of graphite flakes-SiCp /matrix composites : Implications in heat sinking design for thermal management applications. Mater Charact 2015;109:107–11.

[37] Ranut P. On the effective thermal conductivity of aluminum metal foams: Review and improvement of the available empirical and analytical models. Applied thermal engineering 2016; 101:496-524.

[38] Hasselman DPH, Bhatt H, Donaldson KY, Thomas JR. Effect of fiber orientation and sample geometry on the effective thermal conductivity of a uniaxial carbon fiber-reinforced glass matrix composite. J Compos Mater 1992;26: 2278–88.

[39] Goodall R, Marmottant A, Salvo L, Mortensen A. Spherical pore replicated microcellular aluminium: Processing and influence on properties. Mater Sci and Eng 2007;465:124-35.

[40] Xue C, Bai H, Tao PF, Wang JW, Jiang N, Wang SL. Thermal conductivity and mechanical properties of flake graphite/Al composite with a SiC nano-layer on graphite surface. Mat and Des 2016;108:250-58.

Figure captions

Figure 1. Scanning electron microscopy (SEM) micrographs: graphite flakes (a); and sodium chloride particles of an 80-100 µm (b) and 355-500 µm (c) average size.

Figure 2. Schematic views of the experimental setup for the permeability measurements (a) and the equipment used for the power dissipation measurements (b).

Figure 3. Composition ternary phase diagrams as a function of compaction pressure (in MPa) in Preforms A (a) and Preforms B (b). The shaded areas represent restricted zones (preforms can have no compositions inside these regions).

Figure 4. (a) Photograph of the C-1 (left) and A-2 (right) samples; (b-g) optical microscopy images of the Al/Gf foams C-3 (b,e), B-3 (c, f) and KK-3 (d, g, h). In (h), a merely physical contact between various graphite flakes on a layer of the KK-3 sample are observed.

Figure 5. (a) Experimental results of the water volume (m^3) *measured with time (s) by the setup shown in Figure 2(a) for the A-3, C-2 and KK-3 samples - the fitted lines have regression coefficients* $R^2 > 0.99$; *(b) plot of the permeability divided by the square of the average pore diameter* (k/d^2) *versus (1-V´p); (c) a graph of* $\log(K_{mf})$ *versus log(Vm) for the A-1, A-2 and A-3 aluminium foam samples - the straight line fitting the data is:* $\log(K_{mf})=1.5168\cdot\log(Vm)+2.3792$ *and the regression coefficient is* $R^2>0.99$; *(d-e) longitudinal thermal conductivities of the samples in Table 1 versus the volume fraction of pores (d) and the volume fraction of graphite flakes (e).*

Figure 6. (a) Frequency of the average radius of the necks connecting two pores in sample KK-2; the curve was obtained by joining the different experimental results and was extrapolated to the x-axis to read the r_{min} *and* r_{max} *values; (b) -log of both the experimental and calculated permeabilities as a function of V´p -* k_{min} *and* k_{max} *were obtained by accounting for* r_{min} *and* r_{max}*, respectively, in Equation (4).*

Figure 7. Schematic diagrams of the idealized modelling microstructures of the Al/Gf foams fabricated in this work and classified as Model 1 (M1) and Model 2 (M2).

Figure 8. Ternary phase diagrams for the analytical and experimental thermal conductivities of the Al/Gf foams for (a) Model 1; and (b) Model 2.

Figure 9. (a) A graph of the thermal conductivities calculated with M1 (hollow symbols) and M2 (filled symbols) vs. the experimental results for all the samples in Table 1 - the line represents the identity function; (b) the contour curves of the difference in the calculated thermal conductivity resulting from models M2 and M1.

Figure 10. (a) Power density dissipation, and (b) pressure drop of the Al and Al/Gf foams plotted as a function of air flow.

Figure 11. Contour curves of the increment percentage of power dissipation R as function of the thermal conductivity and air flow conditions.

Tables

Table 1. Longitudinal thermal conductivity K_c^L (W m^{-1} K^{-1}) and flexural modulus Ef (GPa) measured for the fabricated Al and Al/Gf foams. D_{NaCl} (μm) is the average of the sodium chloride particles diameter used as a template, P (MPa) is the compaction pressure applied for the preforms conformation and V´f, V´p and V´m denote graphite flakes, pores and metal volume fractions, respectively. k (m^2) and p (g cm^{-3}) are permeability and denisty, respectively.

Material type	Sample code	D_{NaCl}	P	ρ	V´f	V´p	V´m	k	K_c^L	Ef
Al foams	A-1	355-500	0.7	1.18	0.00	0.68	0.32	7.00×10^{-11}	43	5.8
	A-2	355-500	2.0	0.54	0.00	0.78	0.22	5.00×10^{-10}	24	2.1
	A-3	355-500	0.0	0.85	0.00	0.61	0.39	1.30×10^{-11}	57	8.7
Al/Gf foams (Preforms A)	B-1	80-100	2.0	1.60	0.48	0.32	0.20	-	165	-
	B-2	80-100	2.0	1.35	0.30	0.44	0.26	-	125	-
	B-3	80-100	2.0	1.12	0.14	0.56	0.30	-	80	-
	C-1	355-500	2.0	1.48	0.54	0.36	0.10	5.29×10^{-13}	167	1.3
	C-2	355-500	2.0	1.11	0.34	0.52	0.14	8.32×10^{-12}	102	3.2
	C-3	355-500	2.0	0.84	0.16	0.66	0.18	6.80×10^{-11}	60	7.8
	D-1	355-500	0.7	1.52	0.49	0.33	0.18	-	164	-
	D-2	355-500	0.7	1.18	0.32	0.47	0.21	-	115	-
	D-3	355-500	0.7	0.92	0.15	0.60	0.25	-	73	-
Al/Gf foams (Preforms B)	KK-1	355-500	2.5	2.05	0.90	0.06	0.04	4.43×10^{-13}	290	1.5
	KK-2	355-500	2.5	1.40	0.52	0.39	0.09	2.00×10^{-10}	147	1.8
	KK-3	350-500	2.5	1.03	0.30	0.56	0.14	8.00×10^{-11}	70	2.0

Table 2. Different microstructural parameters measured by the image analysis in the indicated samples. N is the coordination number or number of pores in coordination with a given pore through opening connecting windows. r refers to the average size of the opening connecting windows. Subscripts min, max and mode indicate the maximum, minimum and mode values in the distribution of measured r values.

Material type	Sample code	N	r_{min} (μm)	r_{max} (μm)
Al foams	A-1	9	28	66
	A-2	9	55	95
	A-3	9	18	28
Al/Gf foams (Preforms A)	C-1	4	10	35
	C-2	5	20	53
	C-3	6	30	65
Al/Gf foams (Preforms B)	KK-1	4	45	85
	KK-2	4	62	120
	KK-3	4	58	120

Authorship of the paper

The authors have contributed equally to the following tasks that have led to the culmination of this work: conception of the main ideas, experimental data acquisition, validation and writing both the original draft and the revised version of the present manuscript. J.M. Molina has had the role of supervisor and project administrator.

Highlights

A new family of aluminium-based composite foams for thermal management was designed, fabricated and characterized

Two microstructures were developed: i) aluminium foams with graphite flakes in struts; ii) alternating layers of flakes and aluminium foam

Incorporation of oriented graphite flakes into aluminium foams raised outstanding high thermal conductivities of up to 290 W/mK

The power dissipation measured in dynamic condition was up to 325% higher than conventional aluminium foams

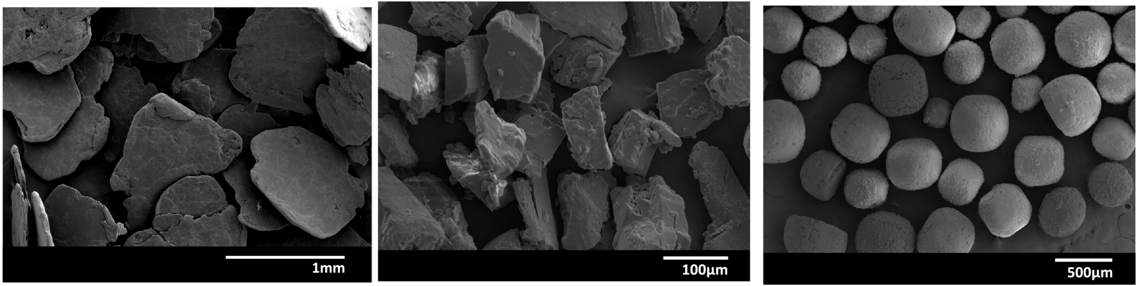

(a) (b) (c)

Figure 1

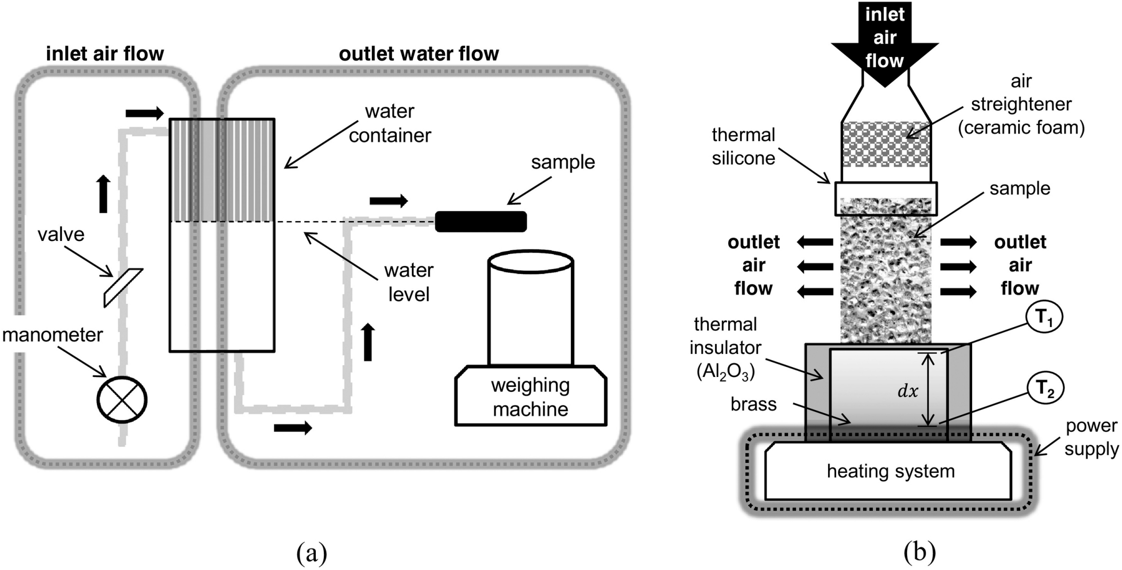
inlet air flow
outlet water flow
water container
sample
valve
water level
manometer
weighing machine
(a)
inlet air flow
air streightener (ceramic foam)
thermal silicone
sample
outlet air flow
outlet air flow
T1
thermal insulator (Al2O3)
dx
T2
brass
power supply
heating system
(b)

Figure 2

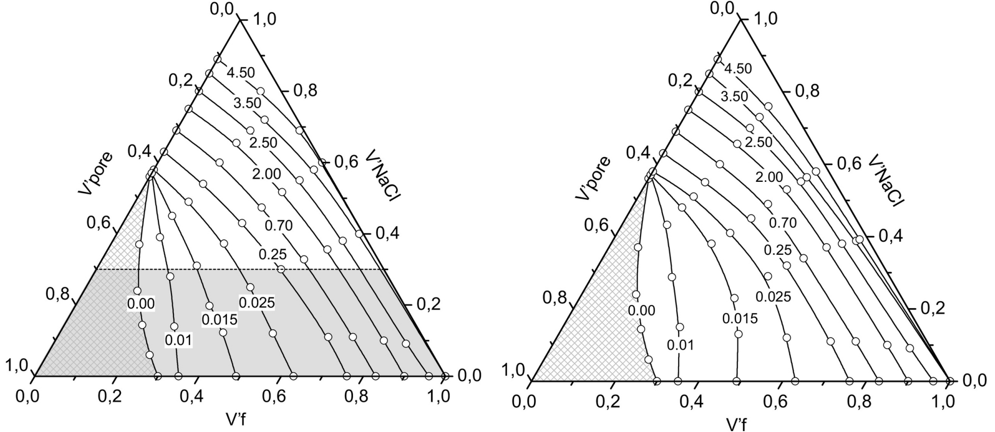
0,0
1,0
0,2
0,8
0,4
0,6
0,6
0,4
0,8
0,2
1,0
0,0
0,0
0,2
0,4
0,6
0,8
1,0
V'pore
V'NaCl
V'f
4.50
3.50
2.50
2.00
0.70
0.25
0.025
0.015
0.01
0.00

(a)

(b)

Figure 3

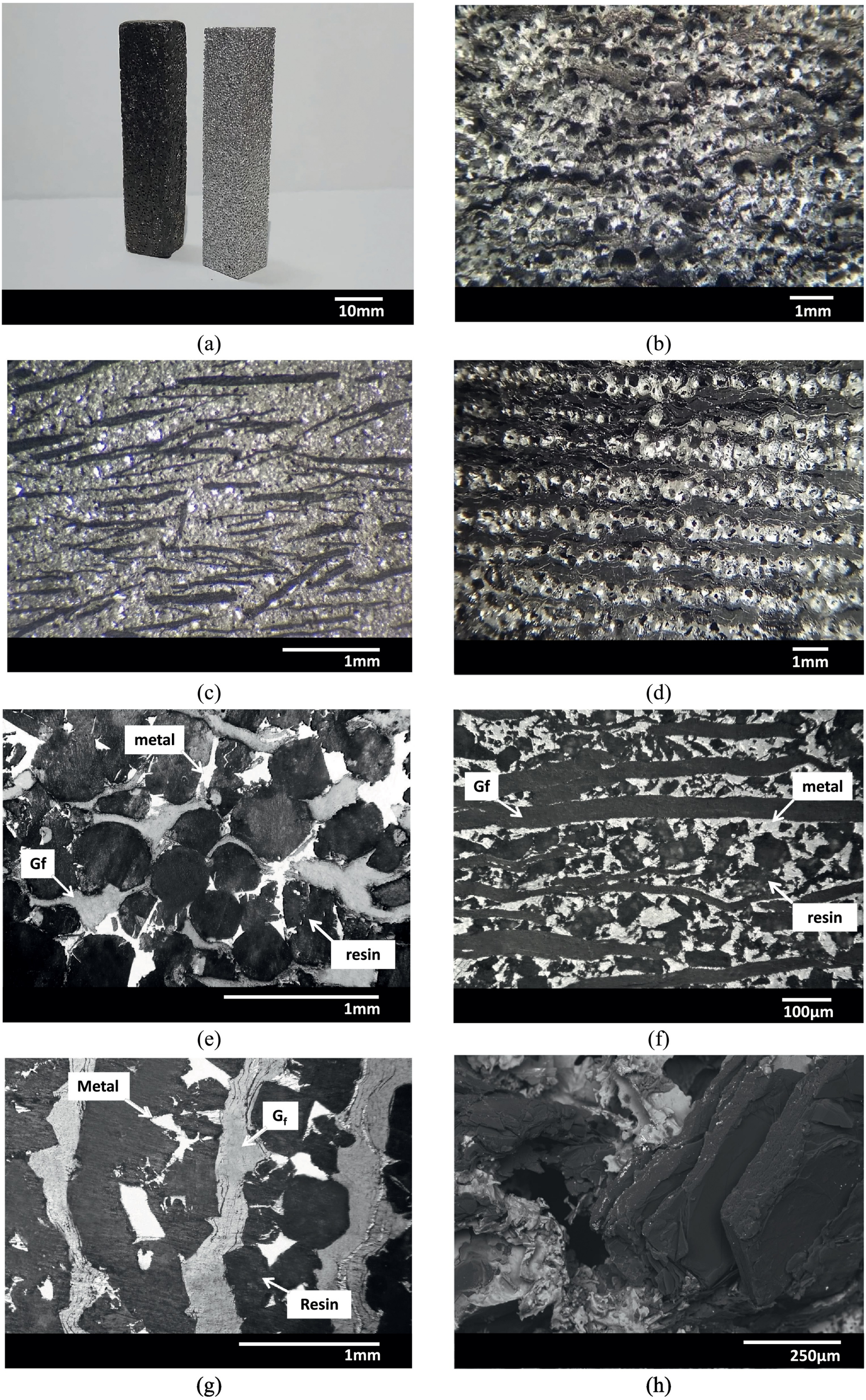
10mm
(a)
1mm
(b)
1mm
(c)
1mm
(d)
metal
Gf
resin
1mm
(e)
Gf
metal
resin
100µm
(f)
Metal
G$_f$
Resin
1mm
(g)
250µm
(h)

Figure 4

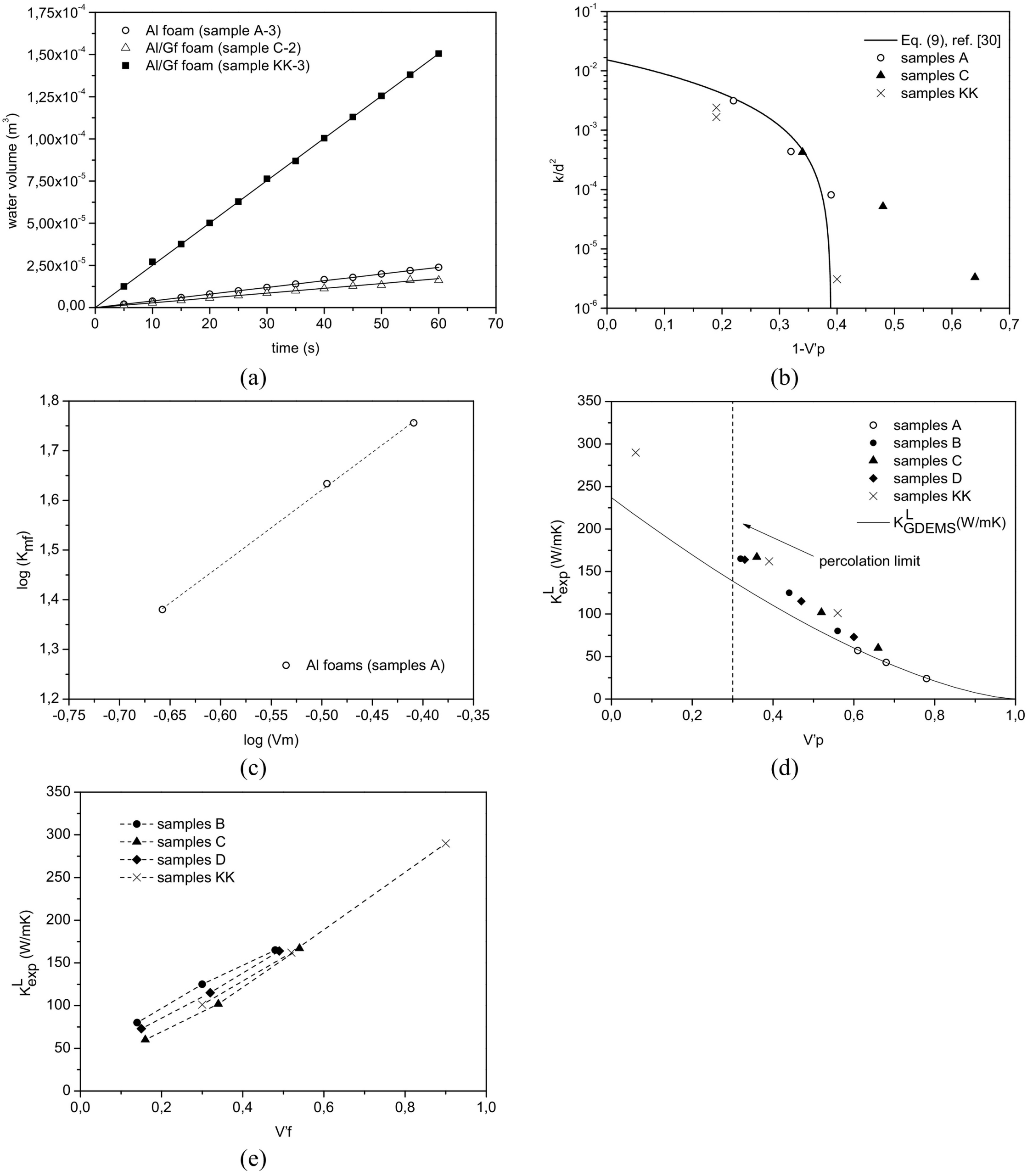

(a)

(b)

(c)

(d)

(e)

Figure 5

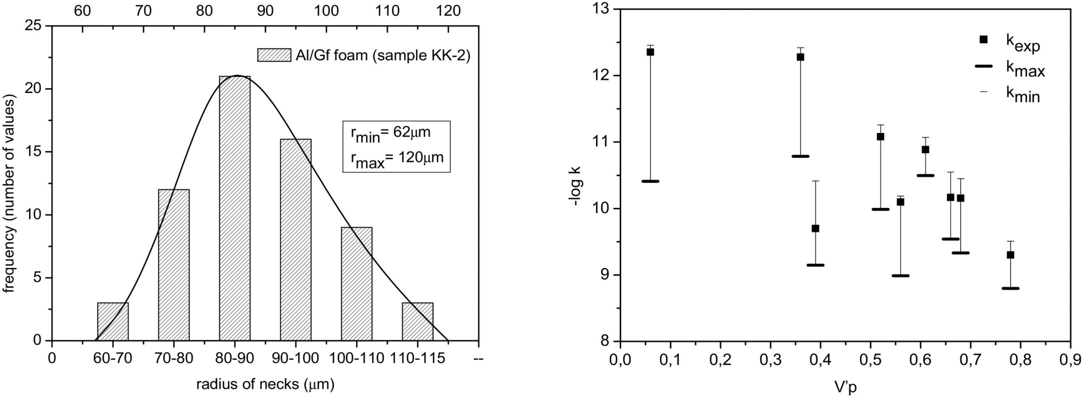
60
70
80
90
100
110
120
25
20
15
10
5
0
frequency (number of values)
Al/Gf foam (sample KK-2)
r_{min}= 62µm
r_{max}= 120µm
0
60-70
70-80
80-90
90-100
100-110
110-115
--
radius of necks (µm)
13
12
11
10
9
8
-log k
k_{exp}
k_{max}
k_{min}
0,0
0,1
0,2
0,3
0,4
0,5
0,6
0,7
0,8
0,9
V'p

(a) (b)

Figure 6

Model 1 (M1): ternary system with homogeneous distribution of oriented Gf

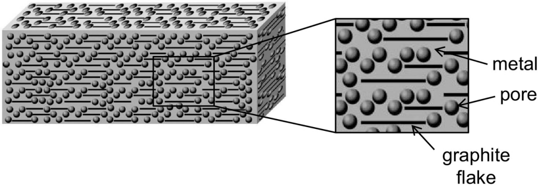

Model 2 (M2): ternary system with alternated layers of Al foam and oriented Gf

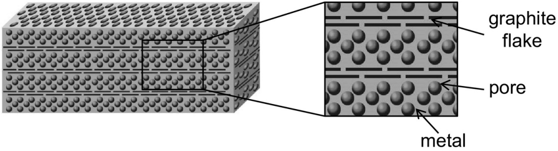

Figure 7

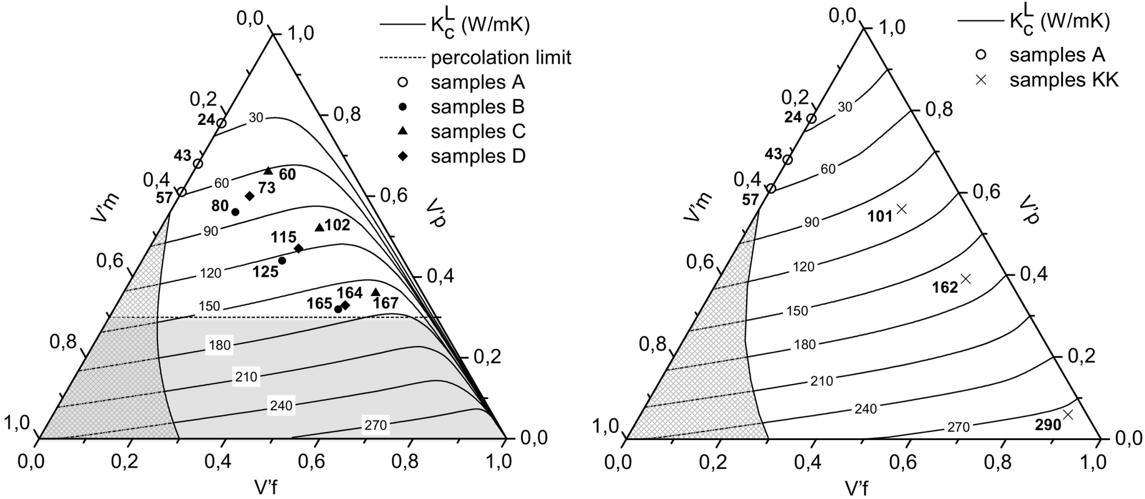
K$_c^L$ (W/mK)
percolation limit
samples A
samples B
samples C
samples D
samples KK
V'f
V'm
V'p
0,0
0,2
0,4
0,6
0,8
1,0
30
60
90
120
150
180
210
240
270
24
43
57
60
73
80
102
115
125
164
165
167
101
162
290

(a)

(b)

Figure 8

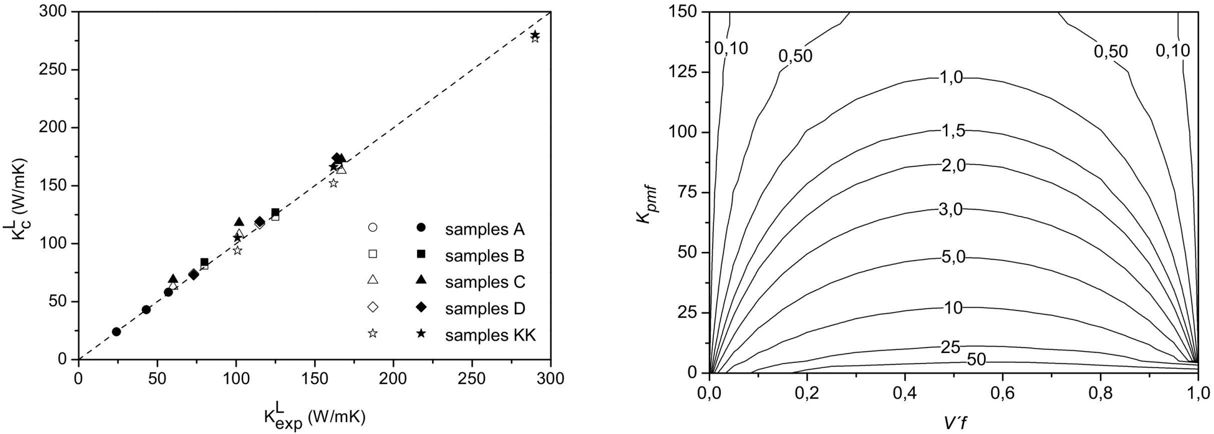300
250
200
150
100
50
0
K_C^L (W/mK)
0
50
100
150
200
250
300
K_{exp}^L (W/mK)
○ ● samples A
□ ■ samples B
△ ▲ samples C
◇ ◆ samples D
☆ ★ samples KK
150
125
100
75
50
25
0
K_{pmf}
0,0
0,2
0,4
0,6
0,8
1,0
V´f
0,10
0,50
0,50
0,10
1,0
1,5
2,0
3,0
5,0
10
25
50

(a)

(b)

Figure 9

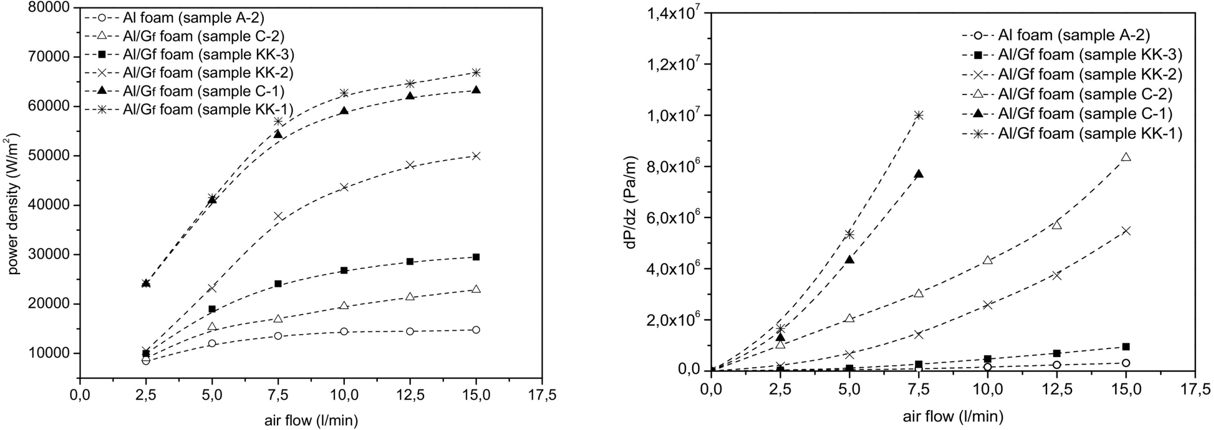
power density (W/m²)
80000
70000
60000
50000
40000
30000
20000
10000
0,0
2,5
5,0
7,5
10,0
12,5
15,0
17,5
air flow (l/min)
Al foam (sample A-2)
Al/Gf foam (sample C-2)
Al/Gf foam (sample KK-3)
Al/Gf foam (sample KK-2)
Al/Gf foam (sample C-1)
Al/Gf foam (sample KK-1)
dP/dz (Pa/m)
1,4x10⁷
1,2x10⁷
1,0x10⁷
8,0x10⁶
6,0x10⁶
4,0x10⁶
2,0x10⁶
0,0
0,0
2,5
5,0
7,5
10,0
12,5
15,0
17,5
air flow (l/min)
Al foam (sample A-2)
Al/Gf foam (sample KK-3)
Al/Gf foam (sample KK-2)
Al/Gf foam (sample C-2)
Al/Gf foam (sample C-1)
Al/Gf foam (sample KK-1)

(a) (b)

Figure 10

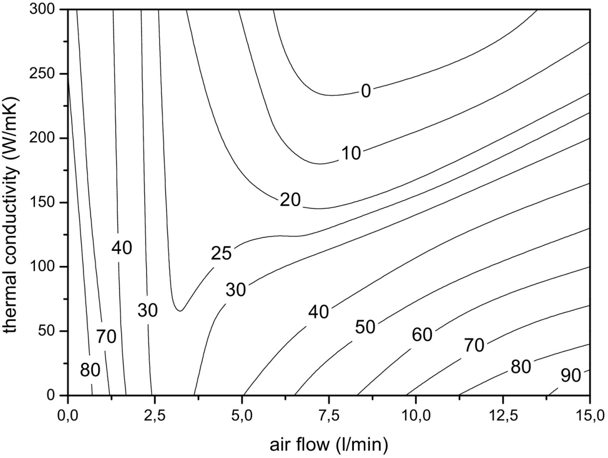
300
250
200
150
100
50
0
thermal conductivity (W/mK)
0,0
2,5
5,0
7,5
10,0
12,5
15,0
air flow (l/min)
0
10
20
25
30
40
50
60
70
80
90
40
30
70
80

Figure 11